RESEARCH ARTICLE

Macromolecular Materials and Engineering Open Access

www.mame-journal.de

Multilayer Hydrogel Microcubes: Effects of Templating Particle Morphology on Cubic Hydrogel Properties

*Daniel Inman, Veronika Kozlovskaya, Pavel Nikishau, Sarah Nealy, Maksim Dolmat, Jonghwa Oh, Claudiu T. Lungu, Lynzi Hunter, and Eugenia Kharlampieva**

Non-spherical stimuli-responsive polymeric particles have shown critical importance in therapeutic delivery. Herein, pH-responsive poly(methacrylic acid) (PMAA) cubic hydrogel microparticles are synthesized by crosslinking PMAA layers within PMAA/poly(*N*-vinylpyrrolidone) hydrogen-bonded multilayers templated on porous inorganic microparticles. This study investigates the effects of template porosity and surface morphology on the PMAA multilayer hydrogel microcube properties. It is found that the hydrogel structure depends on the template's calcination time and temperature. The pH-triggered PMAA hydrogel cube swelling depends on the hydrogel's internal architecture, either hollow capsule-like or non-hollow continuous hydrogels. The loading efficiency of the doxorubicin (DOX) drug inside the microcubes is analyzed by high-performance liquid chromatography (HPLC), and shows the dependenceof the drug uptake on the network structure and morphology controlled by the template porosity. Varying the template calcination from low (300 °C) to high (1000 °C) temperature results in a 2.5-fold greater DOX encapsulation by the hydrogel cubes. The effects of hydrogel surface charge on the DOX loading and release are also studied using zeta-potential measurements. This work provides insight into the effect of structural composition, network morphology, and pH-induced swelling of the cubical hydrogels and may advance the development of stimuli-responsive vehicles for targeted anticancer drug delivery.

1. Introduction

Hydrogels equipped with stimuli-responsive properties have received significant attention due to their advances as therapeutic delivery vehicles. They have been proven essential for biomedicine in gene therapy, tissue engineering, and sensory devices due to their instant reversible transitions in response to internal and external stimuli.[1–3]

Stimuli-responsive properties make unique and novel delivery systems to overcome cytotoxicity, dosing, and direct target delivery challenges.[4–6] For example, photothermal hydrogels with antibacterial properties were fabricated for infected skin wound therapy,[7] wherein near-infrared light-activated carbon nanotubes were embedded to induce hydrogel wound healing properties. Multi-stimuli pH- and enzyme-responsive hydrogels for treating pancreatic cancer displayed effective delivery of gemcitabine by hydrogels compared to current clinical practices involving pure gemcitabine exposure.[8]

The physicochemical properties of hydrogels have been promising in advancing chemotherapy vehicles, but the shape, not fully explored, has been identified as a contributing factor to controlling biophysical interactions.[9,10] For example, rod-shaped particles showed greater susceptibility to micropinocytosis in HeLa and A549 cells than spherical particles for more efficient delivery of therapeutic agents.[11] Prolate ellipsoidal-shaped particles boasted an increased half-life compared to spherical and oblate ellipsoidal particles coated with red blood cells when intravenously injected into mice for extended periods.[12] The curvature in particle geometries has been shown to make them more susceptible to phagocytic internalization, while flat adhesive surfaces reduce internalization, attributing to decreased curvature.[13] The natural complexity of non-spherically shaped biological particles associated with viruses and bacteria is abundant due to natural selection and mutation.[14–16] Therefore, engineering non-spherically shaped nano- and microgels is critical for advancing current understandings of the properties and functioning of particle geometry.

Various techniques to produce non-spherical hydrogel particles have been investigated, including Particle Replication in Nonwetting Templates (PRINT),[17] microfluidics,[18,19] and film

D. Inman, V. Kozlovskaya, P. Nikishau, S. Nealy, M. Dolmat, L. Hunter, E. Kharlampieva
Department of Chemistry
University of Alabama at Birmingham
Birmingham, AL 35294, USA
E-mail: ekharlam@uab.edu

J. Oh
Department of Environmental Health Sciences
University of Alabama at Birmingham
Birmingham, AL 35294, USA

C. T. Lungu, E. Kharlampieva
Center for Nanoscale Materials and Biointegration
University of Alabama at Birmingham
Birmingham, AL 35205, USA

The ORCID identification number(s) for the author(s) of this article can be found under https://doi.org/10.1002/mame.202300284

DOI: 10.1002/mame.202300284

stretching[20,21] leading to non-spherical shapes with controlled sizes, although with challenging scalability and shape variety issues.[22,23] Particles synthesized from film stretching techniques had limited complex diversity in shape, where the viscosity and thickness of poly(vinyl alcohol) were reported to affect the properties of the particle shape.[20] Template-assisted layer-by-layer (LBL) polymer assembly has been proven to be advantageous in the synthesis of shaped gel vehicles where the direct replication of the template is produced by monolayer adsorption of macromolecules to the new surface in multilayer synthesis, providing control over the structure and arrangement of multilayer networks.[24,25] Numerous morphologies and shapes from varying template materials have been investigated,[26,27] with silica and polystyrene widely used to fabricate porous polymer particles by direct templating as they are sturdy, uniform, and readily removable.[28]

Inorganic carbonate templates have also been explored for shaped polymer particle synthesis, where similar properties are displayed; for example, calcium and manganese carbonate templates were used to synthesize polyelectrolyte microcapsules to explore shape-controlled interactions.[29–32] Conjugated hyaluronic acid-dopamine (HA-DOP) and chitosan-polyethylene glycol (CH-PEG) multilayer hydrogels were synthesized using LBL assembly along porous manganese oxide nano-cubes to study the cellular penetration of non-spherical photo/chemotherapy enabled particles for breast cancer cells.[33]

Multilayer hydrogel particles produced on porous templates have reported advanced properties in the structure where hierarchically interconnected cavities allow the 3D structure of particles to remain intact from the polymer infiltration, unlike non-porous templates, where structures collapse upon drying from the hollow interior after template dissolution or removal.[34,35] Conversely, hollow hydrogel capsules have reported great flexibility in solution due to their softness, where the fluid-like interior membrane permits structure recovery from deformations,[36] unlike non-hollow hydrogel particles, where their interconnected architecture and surface properties from filled pores can alter particle mechanical properties.[37]

Capillary and diffusive forces have enhanced the encapsulation properties of non-hollow continuous hydrogel particles due to their available free volume at the network interior, aiding the entrapment of guest molecules.[30] In contrast, capsule-like architectures of particles might be limited in their drug encapsulation mostly to the hydrogel wall. Therefore, studies exploring the extent of particle architectures for efficient encapsulation are necessary to understand integrated properties in shaped particles. Herein, we synthesized non-spherical cubic hydrogel particles with hierarchical architectures using the templated assembly of hydrogen-bonded polymers, poly(methacrylic acid) (PMAA), and poly(*N*-vinylpyrrolidone) (PVPON).[38–40] The assembly of (PMAA/PVPON) bilayers was performed on porous inorganic manganese oxide templates, and the polymeric $(PMAA/PVPON)_5$ replicas of the template porous structure were produced upon template dissolution. The $(PMAA)_5$ multilayer hydrogels replicating the templating particles were synthesized by the chemical crosslinking of PMAA layers with ethylenediamine (EDA) followed by PVPON release from the network at high pH = 8.

We explored the effects of template architecture, including porosity and the presence of a hollow interior, on the properties of 5-layer PMAA multilayer hydrogel microcubes, including their shape stability in the dry state, hydrogel swelling, and the anticancer drug, doxorubicin (DOX), encapsulation and release from the hydrogels. We hypothesized that varying the template calcination temperature from a low (300 °C) to a middle (650 °C) and high (1000 °C) range allows for control over the integrated porous morphology replicated by the PMAA cubic hydrogels. The porous morphology was investigated by scanning electron microscopy (SEM) and atomic force microscopy (AFM), and the material porosity was determined by Brunauer–Emmett–Teller (BET) analysis. In cubical hydrogels analyzed by SEM, the particle swelling ratios were determined using optical microscopy, and hydrogel particle responses in solutions at neutral (pH = 5) and basic pH (pH = 8.5) values were compared to understand the differences in the hydrogel architecture and extension of porosity. Finally, the encapsulation and release of DOX from the hollow and non-hollow hydrogel networks were explored using high-performance liquid chromatography (HPLC) to understand the effect of the cubic hydrogel particle architectures on drug loading and release efficiency. Our findings can be helpful in the development of non-spherically shaped hydrogel microparticles with intelligent hierarchical architectures for highly efficient and stimuli-responsive drug delivery carriers.

2. Results and Discussion

2.1. Synthesis of Porous Inorganic Templates

To obtain cubic hydrogel microparticles, we used the templated LbL assembly of hydrogen-bonded polymers of PMAA and PVPON, as we demonstrated earlier (**Figure 1**).[40,41] First, we synthesized cubic inorganic particles of $MnCO_3$ with an average size of 3.3 ± 0.3 µm (Figure 1a, Figure S1, Supporting Information) using the two-step procedure described previously.[41,42]Solid manganese carbonate cubic microparticles were calcined in a muffled oven at 300, 650, and 1000 °C for 3.5 h to introduce the porous morphology (Figure 1b). The particles were exposed to poly(ethyleneimine) (PEI) from an aqueous solution for 30 min to adsorb PEI onto particle surfaces. The PEI priming was necessary to facilitate the following adsorption of PMAA through ionic interaction between PEI and PMAA.[43] PMAA and PVPON polymers were alternatingly infiltrated into PEI-coated templates at pH = 2 until five bilayers of (PMAA/PVPON) were adsorbed on the pore surfaces through the LBL polymer assembly (Figure 1c,d). After the sacrificial inorganic templates were dissolved in concentrated acid solutions (8 M) of hydrochloric acid, $(PMAA/PVPON)_5$ hydrogen-bonded cubic particles were synthesized (Figure 1e). Finally, the PMAA layers within the physically paired $(PMAA/PVPON)_5$ hydrogen-bonded network were chemically crosslinked with EDA using carbodiimide chemistry.[44] The exposure of the cubic hydrogen-bonded particles to pH = 8 resulted in the swelling of the PMAA network and the release of non-bound PVPON (Figure 1f).[40,41]

The obtained (PMAA) hydrogel particles have a complex hierarchical architecture. The hydrogel network is created on the nanoscale level through a multilayer arrangement of chemically linked PMAA layers. However, the PMAA multilayer coats the

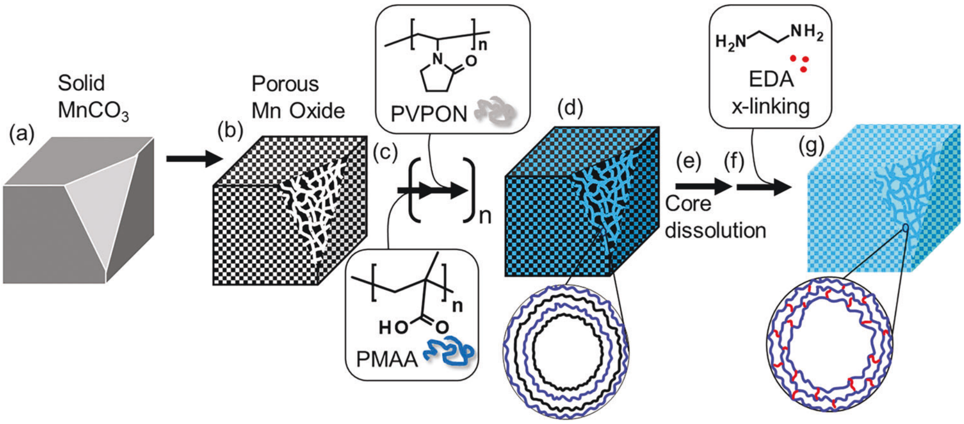

Figure 1. Schematic representation for the synthesis of cubic PMAA multilayer hydrogel microparticles. a) Cubic solid manganese carbonate $MnCO_3$ microparticles were calcined at high temperatures to obtain porous b) cubic microparticles. c) A multilayer of hydrogen-bonded $(PMAA/PVPON)_5$ polymer layers was assembled through an LbL polymer assembly on the d) surfaces of the particle pores. e) After inorganic particle dissolution f) followed by crosslinking of PMAA layers with ethylenediamine (EDA), g) porous cubic hydrogel microparticles (hydrogel microcubes) were obtained. The particle hydrogel network comprised a $(PMAA)_n$ multilayer hydrogel with $n = 5$.

interconnected surfaces of many template pores, replicating the shape and porous architecture of the template on the microscale. Remarkably, when the template is dissolved, additional free volume is obtained in the former spaces of the dissolved inorganic material, which can drastically affect the pH-responsive volume transitions of the hydrogel microparticle and its surface area. Therefore, controlling the initial morphology of the inorganic template can be used to control the swelling/deswelling of the PMAA hydrogel cubes and their drug encapsulation efficiency.

Thus, we explored the effects of the calcination temperature of $MnCO_3$ inorganic templates on the resultant particle morphology. The initial manganese carbonate cubic microparticles were calcined in an oven at 300, 650, and 1000 °C for 3.5 h, and their surface morphology was analyzed using SEM. SEM images in **Figure 2** demonstrate the appearance of pores on the particle surfaces after heating. While particle templates exposed to heat treatment at 300 °C showed relatively smooth surfaces without apparent porosity (Figure 2a), similar to the manganese carbonate starting material (Figure S1, Supporting Information), the $MnCO_3$ templates treated at 650 °C (Figure 2b) and 1000 °C (Figure 2c) displayed a formation of distinguished porous structures with a drastically increasing pore size. The pore opening sizes were estimated to be 10–30 nm and 100–300 nm for the template calcined at 650 and 1000 °C, respectively (Figure 2b–c).

AFM analysis of the calcined particle morphology confirmed the increasing pore size upon the increase in the calcination temperature from 300 to 1000 °C (**Figure 3**a–c). The AFM topography image with a 1 μm^2 scan area of the $MnCO_3$ template calcined at 300 °C revealed the presence of nano-porosity at the particle surfaces with an estimated pore opening size of less than 10 nm (Figure 3a). Gravimetric analysis of $MnCO_3$ templates revealed an increasing particle weight loss from ≈7% at 300 °C to ≈38% at 650 °C and ≈40% at 1000 °C. The weight loss is due to a chemical transformation of manganese carbonate to manganese oxides and the release of carbon oxide and carbon dioxide.[45] The pore size evolution can also occur due to material fusion during manganese carbonate degradation. Thus, previous studies showed that manganese oxide species can have both growing pores and grain sizes when the exposure temperature is raised from 350 to 800 °C through calcination and annealing methods.[46,47] Our SEM and AFM data on the pore and grain sizes of the calcined templates demonstrate the increasing sizes of both features with

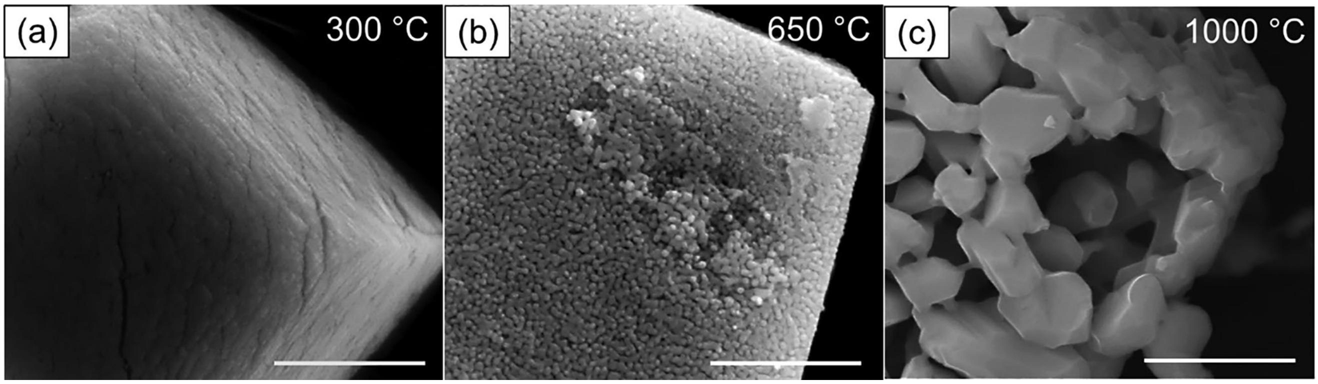

Figure 2. SEM images of cubical porous microparticles obtained by calcining cubical manganese carbonate nonporous microparticles at a) 300 °C, b) 650 °C, and c) 1000 °C for 3.5 h. The scale bar is 1 μm.

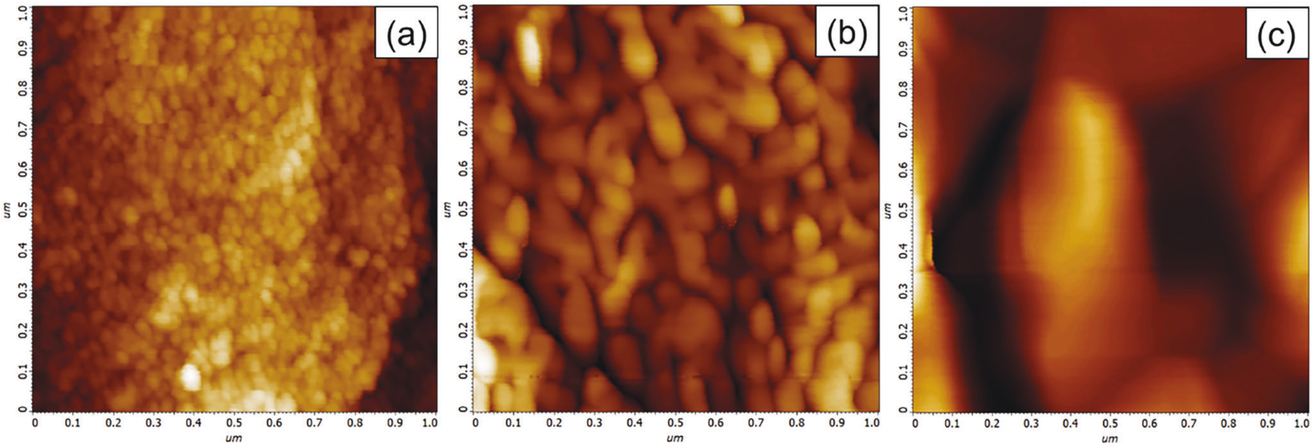

Figure 3. AFM topography images of cubical porous microparticles obtained by calcinating cubical manganese carbonate nonporous microparticles at a) 300 °C, b) 650 °C, and c) 1000 °C for 3.5 h. The scan size is 1 µm. The z-scale is a) 25 nm, b) 61 nm, and c) 165 nm.

the temperature rise from 300 to 1000 °C using the same annealing time (3.5 h).

Unlike previously reported studies involving silicon carbide in aluminum matrix composites, which showed insignificant changes in the percentage of porosity when calcination times were extended from 2–8 h,[48] we observed an increase in the particle surface roughening and changes in particle surface porosity when the annealing time was increased from 1 to 9 h at the calcination temperature of 650 °C (**Figure 4**). The SEM analysis showed that the grain size of the porous surface decreased initially when the calcination time was increased from 1 to 6 h (Figure 4a,b) but started increasing when the calcination time was extended to 9 h of particle heating at 650 °C (Figure 4c). Interestingly, the cubic particle also smoothened, with an

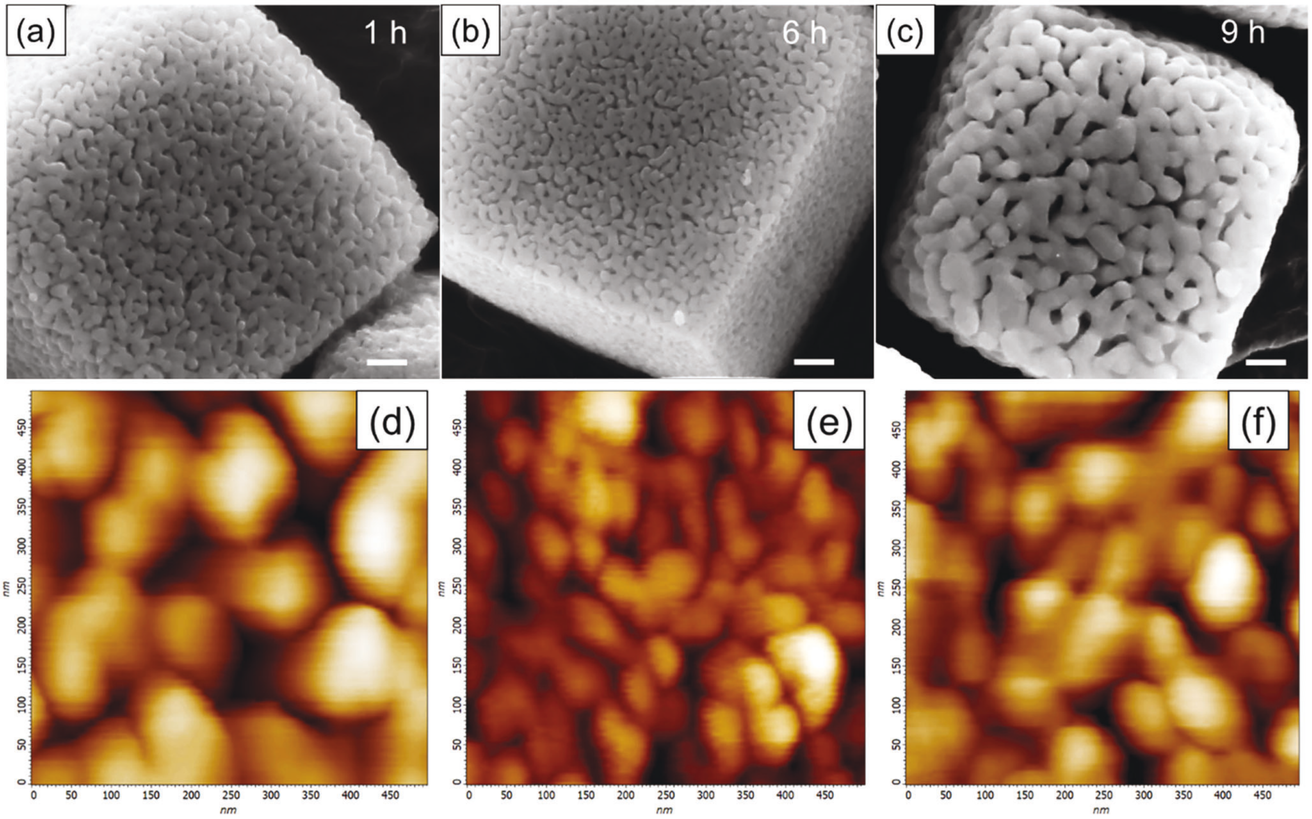

Figure 4. a–c) SEM images of cubical porous microparticles obtained by calcination of cubical manganese carbonate nonporous microparticles at 650 °C for a) 1 h, b) 6 h, and c) 9 h. The scale bar is 250 nm. d–f) AFM topography images of porous templates calcinated at 650 °C for d) 1 h, e) 6 h, and f) 9 h. The scan size is 500 nm, and the z-scale is d) 57 nm, e) 19 nm, f) 46 nm.

Table 1. Average pore size, surface area, and total pore volume of the cubic calcined inorganic microparticles.

Calcination T [°C]	Average pore size [nm]	BET surface area [m^2 g^{-1}]	Total pore volume [cm^3 g^{-1}]
300 @ 3.5 h	5.5 ± 0.1	20.8 ± 0.3	0.0286 ± 0.0005
650 @ 1 h	45.0 ± 3.0	13.5 ± 0.8	0.151 ± 0.001
650 @ 3.5 h	44.1 ± 0.6	12.3 ± 0.3	0.135 ± 0.004
650 @ 6 h	36.4 ± 0.4	10.4 ± 0.2	0.0948 ± 0.0005
650 @ 9 h	41.5 ± 0.8	10.9 ± 0.2	0.114 ± 0.004

evident loss of defined edges at calcination times longer than 6 h (Figure 4c).

These observations are also confirmed by AFM imaging of the particle surface morphology (Figure 4d–f). The grain size analysis of the AFM topography images of the particle surfaces revealed that the average grain size decreased from 137 ± 17 nm to 65 ± 13 nm when the calcination time was increased from 1 to 6 h (Figure 4d,e) but then it increased again to 97 ± 15 nm with three more hours of calcination at 650 °C (Figure 4f). These results agree with the calcination data for the particles annealed at the increasing temperature (Figure 3). The increasing grain size, either through the calcination temperature rise or an increase of the calcination time at the same annealing temperature, can be explained by the initially slow $MnCO_3$ degradation at lower annealing temperatures and a shorter calcination time. At higher temperatures and longer heating times at around 700 °C, the decreased "islands" of material start compacting through sintering.[49]

BET analysis (**Table 1**) revealed that the porous templates had average pore sizes increasing from 5.5 ± 0.1 nm to 44.1 ± 0.6 nm when the calcination temperature was increased from 300 to 650 °C with the corresponding twofold decrease in the surface area from 20.8 ± 0.3 to 12.3 ± 0.3 m^2 g^{-1} due to disappearing the micropores with a greater specific surface area the formation of mesopores with a smaller specific surface area.[50] The increased calcination temperature also increased total pore volume, from 0.0286 ± 0.0005 to 0.135 ± 0.004 cm^3 g$^{-1,}$ with the growth of many pores. Earlier studies on porous materials reported growth in pore sizes from 5 to 32 nm when heating manganese species between 350 and 700 °C,[47–55] which agrees with our findings. We could not characterize the porosity of the microparticle templates calcined at 1000 °C because of their fragility and excessive decomposition throughout the manganese carbonate framework.

The time-dependent calcination of the manganese oxide cubic templating microparticles showed, on average, similar pore sizes of 45 ± 3 nm, 44.1 ± 0.6 nm, 36.4 ± 0.4 nm, and 41.5 ± 0.8 nm after 1, 3.5, 6, and 9 h of calcination at 650 °C (Table 1). However, we observed a decrease in the average BET surface areas, from 13.5 ± 0.8 m^2 g^{-1} to 12.3 ± 0.3 m^2 g^{-1} and 10.9 ± 0.2 m^2 g^{-1} after 1, 6, and 9 h of calcination at 650 °C, respectively as well as in the average total pore volume from 0.151 ± 0.001 cm^3 g^{-1} (after 1 h) to 0.114 ± 0.004 cm^3 g^{-1} (after 9 h) (Table 1). These results agree with previous reports on the average pore sizes of TiO_2-Al_2O_3 photocatalyst material, which decreased from 16.6 to 13.3 nm when the calcination time was increased from 1 to 3.5 h at 500 °C.[52] This behavior is explained by the incomplete decomposition of material in short calcination times, while longer times lead to the destruction of the porous architecture through sintering.

Table 2. XRD analysis of cubic inorganic microparticles after calcination.

Calcination T [°C]	Composition	Phase %
300 @ 3.5 h	$MnCO_3$	≈100
650 @ 1 h	Mn_3O_4	90.3
	Mn_2O_3	9.7
650 @ 3.5 h	Mn_3O_4	69.5
	Mn_2O_3	30.5
650 @ 9 h	Mn_3O_4	33.5
	Mn_2O_3	66.5
1000 @ 3.5 h	Mn_3O_4	100

Unlike TiO_2-Al_2O_3 materials, our manganese oxide particles did not experience destroyed porous features after 9-h calcination (Figure 4) but rather at temperatures greater than 800 °C (Figure 2c) due to the difference in the material's thermal stability and decomposition properties. Our template porosity properties determined by BET analysis indicate the presence of mesopores and micropores and relatively high surface areas.[53,54] We reported a similar distribution of hierarchical porosity in earlier works with cubic and spherical manganese oxide particles of 2 and 4 µm,[41] where average pore sizes were found to be 44 and 40 nm, respectively, in templates synthesized at 700 °C.

The phase composition of porous templates after calcination was investigated by X-ray powder diffraction. Their X-ray diffraction (XRD) patterns are shown in Figures S2 and S3, Supporting Information. The XRD analysis showed that the samples calcined at 300 °C had almost 100% of the initial $MnCO_3$ composition, while increasing the temperature to 1000 °C led to a 100% Mn_3O_4 phase (**Table 2**). The surface properties of low temperature-annealed templates (300 °C) had very low roughening after the treatment (Figures 2a and 3a) and maintained the same chemical composition of $MnCO_3$. Their porosity detected by AFM and BET analysis was obtained by the loss of bound water to the material during the heating at the temperature below the decomposition threshold for manganese carbonate.[55] Time-dependent templates calcined at 650 °C for 1, 3.5, and 9 h demonstrated the presence of Mn_3O_4 and Mn_2O_3 mixtures with extenuating calcination processes (Table 2). These phase transitions agree with literature findings explained by the reduction route and conversion of manganese carbonate when heated between 400 and 1100 °C, where distortions in the phase symmetry between tetrahedral and octahedral sites can occur.[56–58]

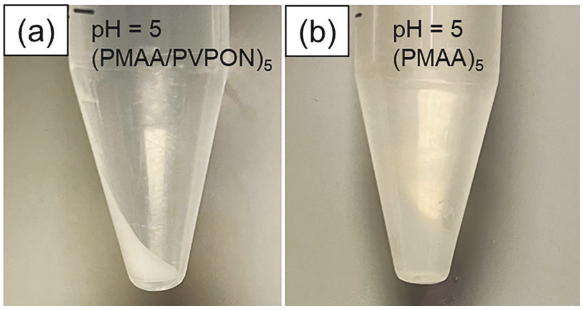

Figure 5. Photographic images of solutions with a) (PMAA/PVPON)$_5$ hydrogen-bonded cubic particles at pH = 5 before crosslinking and b) (PMAA)$_5$ multilayer hydrogel microcubes at pH = 5 after crosslinking and PVPON release.

The obtained manganese oxide compositions can be dissolved in solutions of HCl with high concentrations of the acid and, therefore, were used to investigate the effects of the particle morphology on the properties of the corresponding PMAA multilayer hydrogel inverted replicas of the templates.

2.2. Synthesis of Multilayer Hydrogel Microcubes

After core dissolution in hydrochloric acid (Figure 1e), (PMAA/PVPON)$_5$ hydrogen-bonded cubic particles were produced (**Figure 5**a). Crosslinking of PMAA layers within the 5-bilayer multilayer and a subsequent release of uncrosslinked PVPON at pH = 8 (Figure 1f-g) resulted in the multilayer hydrogel cubes of (PMAA)$_5$ network (Figure 5b). The optical images in Figure 5 demonstrate that more transparent material is obtained after PVPON release and swelling of the PMAA network in solution.

SEM analysis of the hydrogel microparticles dried on silicon wafer surfaces revealed drastically different 3D shapes and surface morphology of the (PMAA)$_5$ hydrogel cubes obtained from the templates calcined at 300, 650, and 1000 °C (**Figure 6**a–c). The hydrogel cubes made from 650 °C-calcined particles were the only ones that maintained their 3D shape after drying (Figure 6b). The hydrogels from 300 °C-calcined templates collapsed on the surfaces, displaying a thick-wall capsule-like structure (Figure 6a). When dried, the hydrogel cubic replicas of the 1000 °C-calcined templates demonstrated very rough surfaces with partially collapsed cubic shapes (Figure 6c). Interestingly, the hydrogels obtained from the templates calcined at 650 °C and at varied times demonstrated an increasing dry shape stability with partially collapsed cubic hydrogels at 1 h of 650 °C template annealing (Figure 6d) to completely cubical hydrogel particles at template annealing times longer than 3.5 h (Figure 6b,e,f).

Notably, surface roughening is observed for the dry (PMAA)$_5$ hydrogels made from the microparticles calcined at 650 °C for 9 h (Figure 6f). This finding confirms our observation that increasing template temperature and increasing annealing times at lower temperatures can affect the surface morphology of the resultant hydrogel microparticles. However, in contrast to 300- and 650 °C-calcined porous sacrificial templates, the fragility of 1000 °C-calcined microparticles can lead to partial destruction of the templates and lead to the synthesis of the shapeless hydrogel microparticles with poorly controlled internal structures. Therefore, hydrogel swelling and drug encapsulation and release were investigated on the (PMAA)$_5$ hydrogel microcubes obtained from 300- and 650 °C-calcined inorganic microparticles, denoted as 300- and 650-PMAA hydrogel cubes, respectively.

The 300- and 650-PMAA hydrogel cubes were treated with the ion chelator, ethylenediamine tetraacetic acid (EDTA), to ensure the purity of the hydrogel networks from manganese ions which can coordinate with carboxylic groups of the PMAA network after core dissolution at low pH. The absence of manganese ions in the hydrogel networks was confirmed by energy dispersive spectroscopy analysis (**Figure 7**a), where the major peaks corresponding to manganese can be seen from 6–6.5 KeV before core dissolution, and no manganese peaks are present in the hydrogel microparticles after core dissolution and EDTA treatment.

The 300- and 650-PMAA hydrogel cubes demonstrated a different swelling behavior when exposed to pH = 8 as analyzed by optical microscopy of the hydrogel microcubes in 0.01 м phosphate buffer solutions. Optical images of the hydrogel cubes in Figure 7 show that 300-PMAA hydrogels have a capsule-like structure with a hollow interior and thick capsule walls, while the 650-PMAA hydrogel cubes have a continuous hydrogel network throughout the particle volume without a hollow interior (Figure 7b–e). This finding agrees with SEM analysis of the hydrogel cubes, which showed that 300-PMAA hydrogel microparticles collapsed on the surface upon drying due to the low rigidity of the structure (Figure 6a). Nevertheless, both cubic 300-PMAA and 650-PMAA hydrogel particles preserved their cubic shape in the network's collapsed state in solutions at pH = 5 (Figure 7b,d) and upon increasing particle sizes in solutions at pH = 8 due to the PMAA network swelling[39,40,41] (Figure 7c,e).

Previously, we demonstrated that (PMAA)$_{13}$ multilayer capsules changed their shape from cubic to bulged spherical-like when exposed to solutions at pH = 5 and 8, respectively.[42] Also, pH-induced swelling of the cubical (PMAA)$_{13}$ hydrogel capsule shell led to partial shape reversibility due to covalent and ionic links in the network.[59] Conversely, the swelling-induced discoidal-to-ellipsoidal shape transformations of (PMAA)$_{15}$ hydrogel capsules with only covalent links in the network showed a complete shape recovery.[60] We also demonstrated that the stiffness of the hydrogel capsule shell was crucial in its shape recovery.[59] For instance, size changes from small-to-large cubical capsules of a more rigid (PMAA-PVPON)$_5$ hydrogel capsule were completely reversible, and the more rigid hydrogel could better withstand the stresses due to pH-triggered swelling. In contrast, the softer (PMAA)$_{20}$ single-component cubical capsule was subject to outward bending of its side faces, and these changes were only partially reversible.[60] In the current work, both hydrogel microparticles demonstrated fully reversible pH-induced size changes and no shape changes upon the network swelling because of the much thicker and, therefore, more rigid architectures of the hydrogel network arranged into a micrometer scale porous structure.

A comparison of the hydrogel swelling ratios calculated as the ratio of the particle size at pH = 8 to that of pH = 5, revealed ≈20% larger swelling of the 650-PMAA hydrogel cubes, unlike the 300-PMAA hydrogel microparticles (Figure 7f). For example, hydrogels from cores produced at 650 °C (3.5 h annealing) displayed a swelling ratio of 1.8 ± 0.2, while hydrogels from 300 °C templates displayed a swelling ratio of 1.6 ± 0.1. This difference

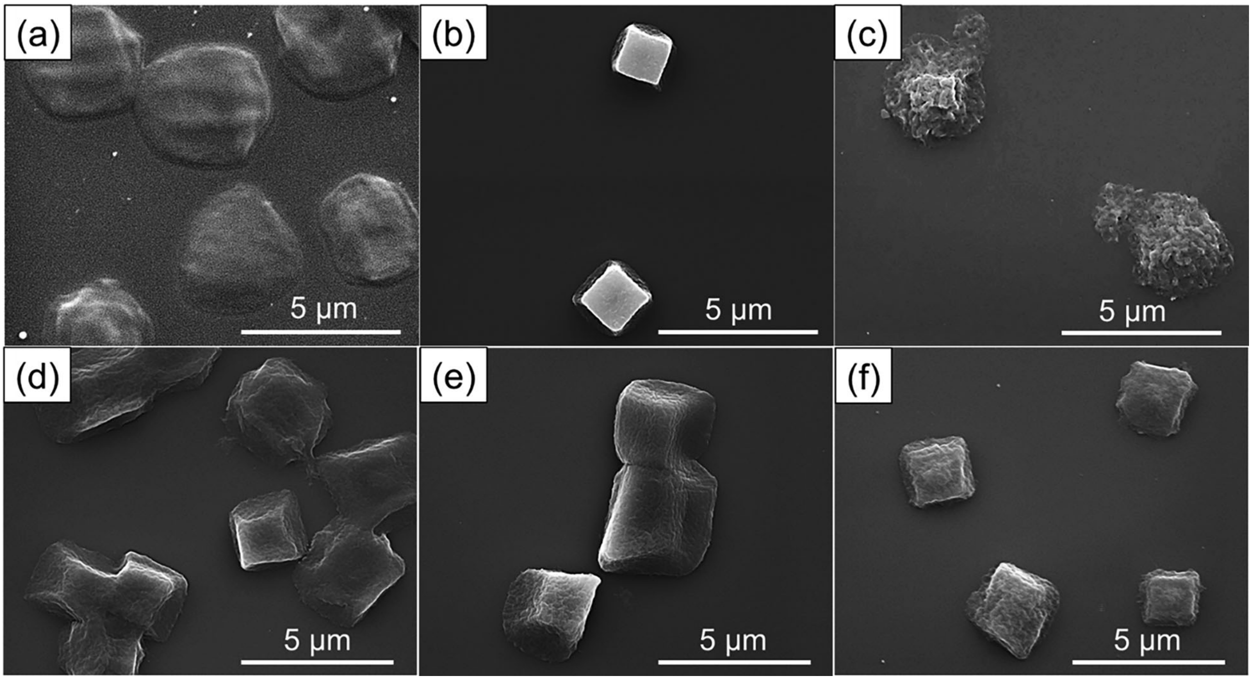

Figure 6. SEM images of $(PMAA)_5$ hydrogel particles obtained using inorganic templates calcined at a) 300, b) 650, and c) 1000 °C for 3 h and calcined at d–f) 650 °C for d) 1 h, e) 6 h, and f) 9 h.

in particle swelling is expected from the hydrogels with different internal architectures with or without a hollow interior

The radii of gyration for PVPON (average M_w 10 000 g mol^{-1}) and PMAA (average M_w 21 000 g mol^{-1}) in solution at pH < 4 can be estimated as 3 and 2.7 nm, respectively, assuming PVPON and PMAA persistence lengths of 1 and 0.3 nm, respectively.[61,62] The corresponding diameters of PVPON (6 nm) and PMAA (5.4 nm) macromolecular coils are comparable with or slightly larger than the average pore size of 300 °C-calcined templates (5.5 ± 0.1 nm), which limits the diffusion of the polymers deeply inside the pores and therefore results in the formation of capsule-like structures with thick walls. On the other hand, the much larger pore size of the 650 °C-calcined templates (36–45 nm) permits the polymer diffusion throughout the porous inorganic particle volume during polymer multilayer deposition and synthesis of the hydrogel particles without a hollow interior. Similarly, capsule-like polymer multilayer particles were reported previously when poly(acrylic acid) was infiltrated into nanoporous silica spheres with decreasing pore size, or PMAA with increasing molecular weight was used in multilayer deposition onto porous particles.[41,63]The hydrogel cubes obtained on the templates calcined at 650 °C for 1–9 h had similar average swelling ratios for the hydrogels from 1-, 3.5-, and 6-h annealed templates (1.8 ± 0.2), while the hydrogel cubes from 9-h treated templates showed a non-significant larger swelling ratio of 2.1 ± 0.3 (Figure S4, Supporting Information).

2.3. Drug Encapsulation and Release by $(PMAA)_5$ Multilayer Hydrogel Cubes

We investigated the effects of $(PMAA)_5$ multilayer hydrogel particle architecture on the encapsulation and release of the anticancer drug DOX. DOX (0.5 mg mL^{-1}) was encapsulated into 300-PMAA- and 650-PMAA-hydrogel particles (**Figure 8**a) by exposing the particle dispersions to the DOX solution in 0.01 M phosphate buffer at pH = 6.4 (Figure 8b). Before the exposure to the hydrogel microparticles, the initial DOX concentration was analyzed with HPLC. After 24-h encapsulation of the drug, the DOX-particle dispersions were centrifuged, and supernatants were analyzed using HPLC, while the resultant DOX-particles were settled (Figure 8c) and rinsed with 0.01 M phosphate buffer solution at pH = 7.4 to remove unbound DOX from solution. The DOX-encapsulated hydrogel cubes were exposed to the acidic solution (pH < 2) for 24 h, and the DOX release from the hydrogel microparticles of different architectures was quantified by HPLC.

As we demonstrated earlier, DOX can be encapsulated by the PMAA multilayer hydrogel at pH = 6.5 due to ionic interactions between positively charged DOX (pK_a = 8.3) and negatively charged PMAA network.[41] Figure 8a demonstrates that at neutral and basic solution conditions (pH > 5), both 300-PMAA- and 650-PMAA-hydrogel cubes acquire a negative surface charge with the zeta-potential values of −25 ± 4 mV and −33 ± 5 mV, respectively. The PMAA network negative charge is because of the ionization of the carboxylic groups in the swollen network at pH > 5.[40,41,45] The zeta-potential of $(PMAA)_5$ hydrogels of both particle types show positive values at acidic conditions (pH = 3) with the corresponding zeta-potential values of 13 ± 2 mV and 22 ± 8 mV for 300-PMAA- and 650-PMAA hydrogels, respectively (Figure 8d), due to protonation of the PMAA carboxylic groups ($pK_a \approx 5$–6) and ionization of one-end reacted crosslinker primary amines in the network ($pK_a \approx 10$).[41] At pH = 5, the surface charge of the hydrogel particles is close to neutral (−9 ± 8 mV for 300-PMAA-hydrogels) or slightly negative (−17 ± 8 mV for 650-PMAA-hydrogels) values due to protonation of most PMAA

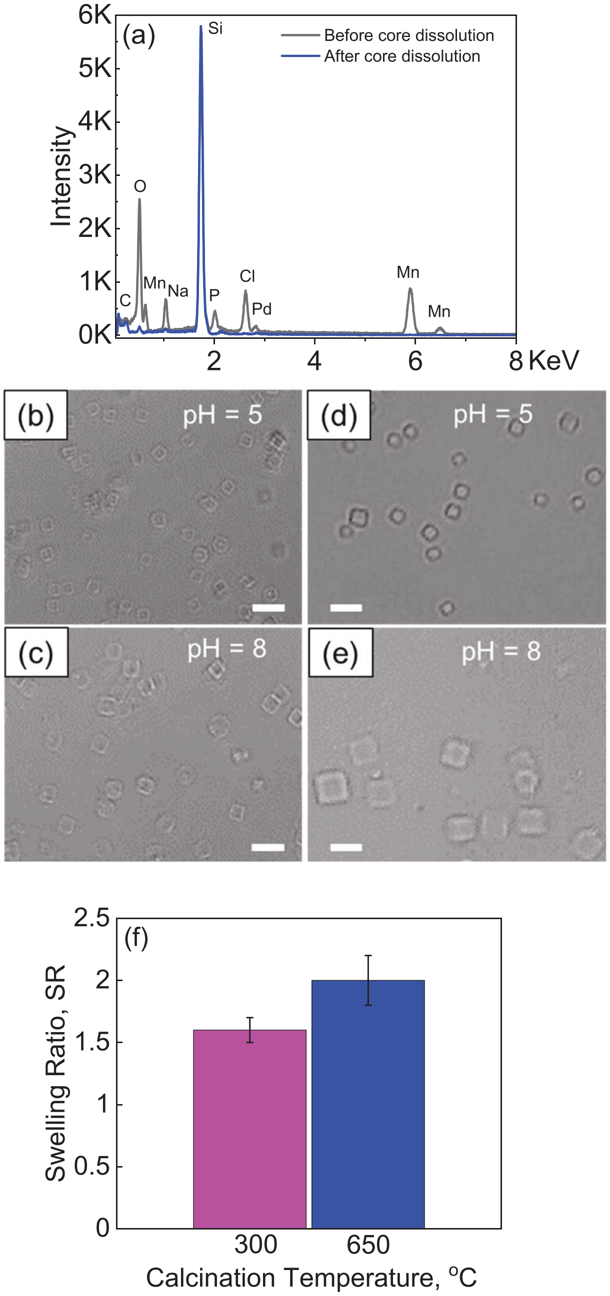

Figure 7. a) Energy dispersive spectroscopy of $(PMAA)_5$ multilayer hydrogel before (black) and after (blue) the template dissolution. b–e) Optical microscopy images of $(PMAA)_5$ hydrogel microcubes in solution at b,d) pH = 5 and c,e) pH = 8. The hydrogels were obtained from the inorganic templates calcined at b,c) 300 °C and d,e) 650 °C for 3.5 h. f) The swelling ratios, SR, of the $(PMAA)_5$ hydrogel microcubes obtained from the porous templates calcined at 300 and 650 °C for 3.5 h. The SR ratio was calculated as the ratio of the particle size at pH = 8 to that of pH = 5.

ionized COO^- groups and their ionic interactions with the positively charged primary amines. The slightly more negative zeta-potential values at pH = 8 and slightly more positive values at pH = 3 for the 650-PMAA-hydrogel cubes may indicate more PMAA network material for this multilayer hydrogel system than that for the 300-PMAA-hydrogel. This observation agrees with the optical microscopy and electron microscopy imaging results that demonstrate the presence of a hollow interior in 300-PMAA-hydrogels. For both types of hydrogel cubes, the pH-dependent changes in the PMAA network charges allowed for DOX encapsulation at pH = 6.5 and a subsequent release at acidic conditions where the network released the drug due to mutual repulsions of excess DOX positive charges.

The typical chromatograms of DOX from the initial DOX solution and after its release from the PMAA hydrogel cubes are shown in Figure 8e. The DOX retention time is 8.83 ± 0.05 min. Due to the high selectivity and insignificant DOX decomposition under the studied conditions, no other components can interfere with the DOX, which can be well detected and quantified in the supernatant samples. HPLC analysis revealed that for both types of hydrogel particles, the loading drug concentration was similar, with 0.5044 ± 0.0441 mg mL^{-1} and 0.5145 ± 0.0171 mg mL^{-1} of DOX for 300-PMAA- and 650-PMAA-hydrogels, respectively. Interestingly, the DOX encapsulation was found to be close to 100% for both types of hydrogel particles and was 99.2 ± 1.4 and 99.5 ± 1.4% for 300-PMAA- and 650-PMAA-hydrogel cubes, respectively. Despite that, the DOX encapsulation per particle was found to be 2.5-fold larger in 300-PMAA-hydrogel cubes than in 650-PMAA-hydrogels with the corresponding values of 9.4 ± 1.5 pg DOX per particle and 3.7 ± 0.2 pg DOX per particle. These loading values are below the maximum theoretical loading (25–35 pg DOX per particle) into a cubical particle with an average size of 2–3 µm.

The fluidic shear stress has been shown to induce dissociation of polymer non-covalent constructs such as micelles,[64] block copolymer complexes with DNA,[65] phospholipid vesicles,[66] or 3-µm nanoparticle aggregates[67] due to high material deformation, resulting in loss of their structure and premature release of their payload due to the disrupted integrity of a nanocarrier. However, the DOX encapsulation in this work does not rely on simple entrapment by a polymeric protective layer, as reported in the above references. The encapsulated DOX molecules are secured within the hydrogel through ionic pairing between the negatively charged PMAA network and positively charged DOX molecules and do not release upon applied centrifugal forces but in response to solution acidity change. The low-speed centrifugation (< 6000 rpm) used in this study was adequate for settling both polymer template and hydrogel particles without disrupting either hydrogen-bonded or electrostatic bonds.

The DOX release was performed at acidic pH for 24 h, where the electrostatic interactions between the PMAA network and the DOX molecules are interrupted by the protonation of COO^- to COOH and the free primary amine groups from EDA and DOX both become positively charged, NH_3^+. The repulsive charge from both amine groups initiates the release of DOX from the network. We used HPLC analysis to find that under these conditions, DOX-loaded 300-PMAA- and 650-PMAA-hydrogels with similar concentrations released 32 ± 8% and 35 ± 4% of encapsulated DOX, respectively.

Therefore, both hydrogel cubes are pH-sensitive and can encapsulate and release DOX upon pH changes. The quantitative differences in the DOX encapsulation per hydrogel particle and the extent of the DOX release can be rationalized not only through the environmental pH changes but also through

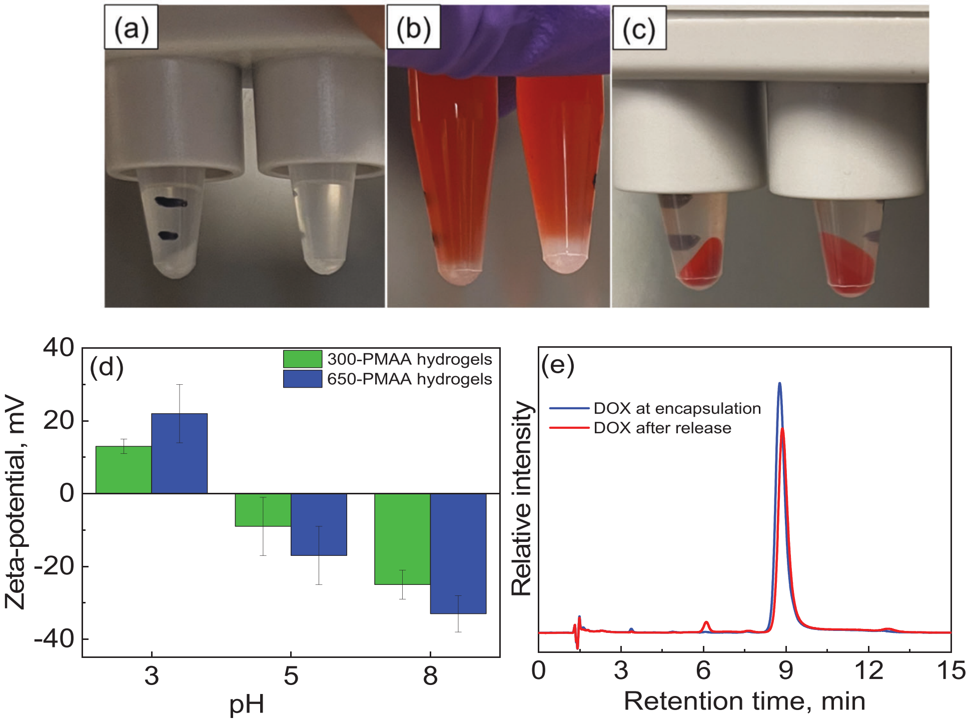

Figure 8. Photo images of (PMAA)$_5$ hydrogel microcube solutions a) before DOX encapsulation, b) upon addition of DOX to the hydrogels, and c) after DOX encapsulation for 24 h and removal of supernatant with non-encapsulated DOX. d) pH-dependent zeta-potential variations of 300-PMAA- and 650-PMAA-hydrogel cubes in solutions at pH = 3, pH = 5, and pH 8. e) Representative HPLC chromatograms of the free DOX containing supernatants as shown in (b), and after DOX release from the hydrogels at acidic pH.

understanding the differences in the architecture and arrangement of a polymer network in the particles contributing to the diffusion of DOX molecules during the encapsulation and release.[68] Thus, the hydrogel particle represents an inverse replica of the inorganic porous template. In contrast to the 650-PMAA-hydrogel particle with no hollow interior, the 300-PMAA-hydrogel also has a microscale hollow cavity inside the hydrogel microparticle. The 2.5-fold larger DOX encapsulation into the PMAA thick-wall cubic hydrogel capsules (200-PMAA-hydrogels) is most probably due to faster diffusion of the drug through a much thinner hydrogel network compared to the continuous, no-hollow interior containing PMAA network. Similarly, at pH lowering, DOX diffuses faster through the 300-PMAA-hydrogel thinner wall than in the case of thick continuous 650-PMAA-hydrogel cubes with, on average, ≈3 pg per particle and 1.3 pg per particle of DOX release from the 300-PMAA- and 650-PMAA-hydrogel cubes after 24 h of exposure to acidic conditions. These results agree with the report by Dong and colleagues,[69] who studied the release of DOX from Salecan/PMAA hydrogel networks and found that the interior architecture of the hydrogels with larger pores better facilitated the release of DOX.

3. Conclusions

We synthesized hydrogel particles of cubic shape with hierarchical architectures using the templated assembly of hydrogen-bonded polymers, PMAA, and PVPON on porous inorganic templates prepared through calcination of cubic nonporous manganese carbonate microparticles of ≈4 µm. The 5-bilayer polymeric (PMAA/PVPON)$_5$ replicas of the template porous structures were produced upon the template dissolution. Chemical crosslinking of PMAA layers within (PMAA/PVPON)$_5$ with EDA and release of PVPON from the (PMAA)$_5$ multilayer hydrogel network at high pH = 8.5 led to the (PMAA)$_5$ multilayer hydrogel cubes replicating the architecture of the templating particles. We explored the effects of template porosity and a hollow interior on the properties of (PMAA)$_5$ multilayer hydrogel cubes, including their dry shape, swelling ratio, and DOX encapsulation and release from the hydrogel cubes. We found that both increasing calcination temperature of manganese carbonate templates from 300 to 650 and 1000 °C or the calcination time from 1 to 9 h at 650 °C resulted in the porous morphology of the produced templates that could be used to synthesize porous hydrogel microcubes with or without hollow interior. The porous templates with increasing average pore sizes from 5.5 ± 0.1 nm to 44.1 ± 0.6 nm were obtained when the calcination temperature was increased from 300 to 650 °C with the corresponding twofold decrease in the surface area from 20.8 ± 0.3 to 12.3 ± 0.3 m^2 g^{-1}.

Conversely, the time-dependent calcination of manganese oxide cubic templating microparticles led to similar pore sizes of 45 ± 3 nm, 44.1 ± 0.6 nm, 36.4 ± 0.4 nm, and 41.5 ± 0.8 nm after 1, 3.5, 6, and 9 h of calcination at 650 °C. In contrast to 300- and 650 °C-calcined porous templates, the 1000 °C-calcined microparticles were found to be highly fragile, and partial destruction of the templates during polymer assembly resulted in shapeless hydrogel microparticles with poorly controlled internal structures. SEM, AFM, and optical microscopy analysis demonstrated that 300-PMAA hydrogels (obtained from 300 °C-calcined inorganic microparticles) have a capsule-like structure with a hollow interior and thick capsule walls. The 650-PMAA hydrogel cubes (obtained from 650 °C-calcined inorganic microparticles) have a continuous hydrogel network throughout the particle volume without a hollow interior. Despite that, cubic 300-PMAA and 650-PMAA hydrogel particles preserved their cubic shape in solutions at $pH = 5$, where the PMAA network collapsed and upon PMAA network swelling when particle sizes increased in solutions at $pH = 8.5$. The $(PMAA)_5$ hydrogel microcube swelling ratios calculated as the ratio of the particle size at $pH = 8.5$ to that of $pH = 5$, showed ≈20% larger swelling of the 650-PMAA hydrogel cubes (1.8 ± 0.2), unlike the 300-PMAA hydrogel microparticles (1.6 ± 0.1). The pH-dependent changes in the PMAA network charges allowed for DOX encapsulation at $pH = 6.5$ and a subsequent release at acidic conditions for both hydrogel microcubes. Remarkably, the DOX encapsulation was 2.5-fold larger in 300-PMAA-hydrogel cubes than in 650-PMAA-hydrogels with the respective values of 9.4 ± 1.5 pg and 3.7 ± 0.2 pg DOX per particle. The 2.5-fold larger DOX encapsulation into the PMAA thick-wall cubic hydrogel capsules (300-PMAA-hydrogels) is due to faster diffusion of the drug through a much thinner hydrogel network compared to the continuous, no-hollow-interior 650-PMAA hydrogel cubes. Similarly, at acidic pH, DOX released faster from the thinner 300-PMAA-hydrogels after 24-h exposure than that for thick continuous 650-PMAA-hydrogel cubes with ≈3 pg DOX per particle and 1.3 pg DOX per particle for the 300-PMAA- and 650-PMAA-hydrogel cubes, respectively. Our results demonstrate that the internal architecture of the hydrogel microcubes can be controlled by controlling the calcination of the initial solid manganese oxide microcubes and is crucial for the functional behavior of both types of pH-sensitive PMAA multilayer hydrogels. The hydrogel architectural differences can be useful for different types of drug delivery, including fast burst-like or slow, sustained therapeutic delivery. Our findings can also contribute to developing non-spherically shaped hydrogel microparticles with intelligent hierarchical architectures for highly efficient and stimuli-responsive drug delivery carriers.

4. Experimental Section

Materials: Ammonium bicarbonate, manganese sulfate monohydrate, ethylenediamine tetraacetic acid sodium salt (EDTA), and mono- and dibasic sodium phosphate used to prepare buffer solutions were purchased from Fisher Scientific. PEI (average M_w 25 000 g mol^{-1}), PMAA (average M_w 21 000 g mol^{-1}), PVPON (average M_w 10 000 g mol^{-1}) and EDA, 2-propanol were acquired from Sigma-Aldrich. NH_4HCO_3 and $MnSO_4$ were from Fisher Scientific. 1-ethyl-3-(3-(dimethyl amino)propyl)carbodiimide hydrochloride (EDC) was received from Chem-Impex International. DOX hydrochloride as powder was received from LC Laboratories (USA). Aqueous 1 м HCl and NaOH solutions were used to control solution pH. Ready-to-use Float-A-Lyzer dialysis devices with MWCO 3.5 and 20 kDa were from SpectrumLabs. All experiments used deionized (DI) water with a resistivity of 18.2 MΩ cm^{-1} (Evoqua).

Synthesis of Porous Cubic Microparticles: Micrometer-sized cubic manganese carbonate ($MnCO_3$) cores were synthesized as described previously.[70] A nano-seed solution was prepared first by mixing NH_4HCO_3 (0.02 g) and $MnSO_4$ (0.01 g) in 50 mL DI water, followed by filtering. Then 50 mL of the nano-seed solution was added to a 2 L aqueous solution containing 1 L of 6 mм $MnSO_4$ and 1 L of 0.06 м NH_4HCO_3, both having 0.5 vol% 2-propanol. The mixture was incubated at 45 °C for ≈1 h until some turbidity started to form. Synthesized $MnCO_3$ microparticles were collected by filtration using 0.8 µm nitrocellulose membrane filters (Fisher Scientific), rinsed with DI water multiple times, and dried at ambient temperature (≈25 °C) in the vacuum oven overnight. The dried particles were calcined in a muffle oven (Thermo Scientific) at 300, 650, and 1000 °C to obtain porous manganese oxide cubic particles.

Synthesis of Multilayer Hydrogel Particles: First, the PEI monolayer was adsorbed on the surfaces of the porous manganese oxide microparticles (250 mg) from a 1.5 mg mL^{-1} DI water solution for 45 min using a programmable rotator (Rotobot, Benchmark Scientific). The excess polymer solution was removed by centrifugation of the particle dispersion at 4900 rpm for 10 min, followed by rinsing the PEI-modified particles twice with a phosphate buffer solution (0.01 м, $pH = 2.0$). Then, hydrogen-bonded multilayers of PMAA/PVPON were adsorbed on the PEI-modified surfaces of the microparticles from 1.5 mg mL^{-1} polymer solution (0.01 м phosphate buffer, $pH = 2.0$). Sequential layers of PMAA and PVPON were deposited for 30 min each using a Rotobot, with two rinses with 0.01 м phosphate buffer solution at $pH = 2.0$ between each layer. After five bilayers of (PMAA/PVPON) were adsorbed on the surfaces of the PEI-modified microparticles, the inorganic core was dissolved in 8 м HCl for 24 h, followed by two rinses in each solution of 6 and 3 м HCl, and DI water at $pH = 2$. The $(PMAA/PVPON)_5$ polymer replicas of the porous cores were then exposed to an EDC solution (5 mg mL^{-1}, 0.01 м phosphate buffer, $pH = 5.0$) for 30 min to activate carboxylic groups in PMAA, followed by three-time-rinsing with 0.01 м phosphate buffer solution at $pH = 2$ to remove free EDC from particle dispersion. The EDC-treated $(PMAA/PVPON)_5$ polymer replicas were then treated with EDA solution (12 µL mL^{-1}, 0.01 м phosphate buffer, $pH = 5.0$) for 16 h to crosslink PMAA layers followed by a three-time-rinse with 0.01 м phosphate buffer solution at $pH = 5$ to remove unreacted EDA. Afterward, the PMAA-crosslinked polymer particles were exposed to 0.01 м buffer solution at $pH = 8.5$ for 24 h to release PVPON from the PMAA network, followed by rinsing the particles with 0.01 м buffer solution at $pH = 8.5$ two times. The obtained PMAA multilayer hydrogel cubes were left in shaking in 0.1 м EDTA solution ($pH = 7$, DI water) for 24 h, followed by dialysis for 3 days in DI water at $pH = 2$ (adjusted by 0.01 м HCl) using Float-A-Lyzer devices with MWCO 20 kDa. The PMAA hydrogel particles were stored in 0.01 м phosphate buffer at $pH = 5$. PMAA hydrogel particle concentration was measured by adding aliquots of particle suspension to a Hausser Scientific ruled hemocytometer (0.1 mm deep) from Electron Microscopy Sciences.

Optical Microscopy: The polymeric hydrogel particles' size and pH-triggered swelling ratios were analyzed using a Fisherbrand optical microscope with a 40× oil immersion objective. Before imaging, the hydrogel particles were centrifuged and transferred to a 0.01 м phosphate buffer solution of $pH = 3$, 5, or 8.5 to determine pH-dependent changes in cubic particle size/shape. The particles were dispersed by vortex for 30 s at 2500 rpm and transferred to a coverglass (Lab-Tek) for imaging. Five exchanges of the sample solution in the coverglass were made, and the optical microscope images from each solution exchange were collected. Intensity-height profiles of the cubic particle edges were generated with ImageJ software to determine the particle size precisely. Marker lines were drawn through the particle of interest, and the distance between the center of opposite cubic edges was measured. The hydrogel swelling ratios were calculated as the increase in cubic particle size at pH 8.5 compared to pH 5.

Encapsulation and Release of DOX: DOX was encapsulated into hydrogel particles by exposing the particle dispersions to 0.5 mg mL^{-1} DOX solution in 0.01 м phosphate buffer at $pH = 6.5$ for 24 h. The concentration of DOX initial solutions was analyzed with HPLC before exposure to the hydrogel microparticles. Then, 100 µL of swollen particles (0.01 м phosphate buffer, $pH = 6.5$) were placed in a 1.5 mL Eppendorf tube, diluted with the DOX solution to 1.0 mL, covered with aluminum foil, and shaken for 24 h to encapsulate DOX within the hydrogel cubes and resulting in DOX-particles. After that, the DOX-particle dispersions were centrifuged, and supernatants were removed for HPLC analysis. The DOX particles were settled and rinsed five times with 0.01 м phosphate buffer solution at $pH = 7.4$. The DOX release study was performed at $pH \approx 1.6–1.8$ for 24 h by adding 50 µL of 1.0 м HCl to 1.0 mL of particle dispersion. The final dispersion was centrifuge, and supernatants were removed for HPLC analysis.

Particle concentration before DOX loading and release experiments was calculated using an improved Neubauer Hemocytometer (0.1 mm deep, Hausser Scientific) and by adding 10 μL of particle dispersion and diluting, if necessary, to have 50–150 particles per analysis square.

HPLC: The DOX analysis was performed by HPLC on an Agilent 1220 Infinity chromatography system (Agilent) using methanol (60%, v/v), water (39.5%, v/v), and orthophosphoric acid (0.5%, v/v; Fisher Scientific) as mobile phase. 30 μL of DOX solution was injected and separated using Hypersil ODS C18 (Thermo Scientific) HPLC column at a 1.2 mL min^{-1} flow rate and room temperature. Detection was performed using a UV detector with a working wavelength of 255 nm and OpenLab ChemStation software (Agilent).

SEM: SEM analysis of manganese oxide templating microparticles and polymeric particles was performed using an FEI Quanta SEM microscope. For the analysis, manganese oxide microparticles were deposited onto carbon film (TED Pella, 8 mm × 20 m), while PEI(PMAA/PVPON)$_5$-modified template-polymer particles and PMAA multilayer hydrogel cubes were adsorbed onto silicon wafer chips (University Wafer, 0.5 cm × 0.5 cm) and dried at ambient conditions. The dry samples were sputter-coated with ≈1 nm platinum using Denton Vacuum Sputter Coater. Secondary electron Imaging was performed at 10 kV. Energy-dispersive X-ray analysis (EDAX) was performed at 15 kV to analyze the hydrogel particles for manganese ions.

XRD: XRD analysis of cubic inorganic particles was performed using a PANalytical Empyrean Multipurpose X-ray Diffractometer. Samples were prepared by adding particle powder to the 16-mm stage and scanned in triplicate. The divergence slit of ½°, soller slit of 0.04° for incident and divergence beam, respectively, and anti-scatter slit of 2° were used. The analysis was performed using the High-Score Pulse software to assess peaks using the Rietveld refinement technique incorporated in the system.

AFM: The topographical images of inorganic cores and hydrogel particles were obtained using an NTegra NT-MDT atomic force microscope. Mn_2O_3 particles were placed on a carbon tape (TED Pella) that was attached to a silicon wafer chip (0.5 cm × 0.5 cm). Loose particles were removed from the sample by a gentle stream of nitrogen (Airgas). The PMAA hydrogel cubes were drop-cast on a clean, dry silicon wafer and dried for 2 days at ambient conditions. NSG30 probes (10 nm radius; 22–100 N m^{-1} force constant; 240–440 kHz resonance frequency) were used to collect the topography of Mn_2O_3 cores and PMAA cubical hydrogels at a scan rate of 0.5 Hz at room temperature.

BET Analysis: Surface properties, including porosity and surface area, were analyzed for manganese oxide particles by micromeritics ASAP 2020 physisorption. The samples were degassed at 30 °C followed by nitrogen (Airgas) adsorption at −196 °C. BET theory was used to determine surface area, total pore volume, and average pore size at the highest relative pressure.

Supporting Information

Supporting Information is available from the Wiley Online Library or from the author.

Acknowledgements

This work was funded by NSF DMR award #1904816 (E.K.). This material is in part based upon work supported under the IR/D Program by the National Science Foundation (E.K.). Any opinions, findings and conclusions, or recommendations expressed in this material are those of the author(s) and do not necessarily reflect the views of the National Science Foundation.

Conflict of Interest

The authors declare no conflict of interest.

Author Contributions

D.I. and V.K. contributed equally to this work. The manuscript was written through the contributions of all authors. All authors have approved the final version of the manuscript.

Data Availability Statement

The data that support the findings of this study are available from the corresponding author upon reasonable request.

Keywords

multilayer hydrogels, non-spherical particles, particle architecture, porosity, therapeutic delivery

Received: August 11, 2023
Revised: October 2, 2023
Published online: October 24, 2023

---

[1] B. G. Carvalho, F. F. Vit, H. F. Carvalho, S. W. Han, L. G. de la Torre, *Biomacromolecules* **2022**, *23*, 1545.
[2] K. Y. Lee, D. J. Mooney, *Chem. Rev.* **2001**, *101*, 1869.
[3] L. Xu, Y. Chen, M. Yu, M. Hou, G. Gong, H. Tan, N. Li, J. Xu, *Nano Energy* **2023**, *107*, 108119.
[4] P. K. Bolla, V. A. Rodriguez, R. S. Kalhapure, C. S. Kolli, S. Andrews, J. Renukuntla, *J. Drug Delivery Sci. Technol.* **2018**, *46*, 416.
[5] A. Bratek-Skicki, *Appl. Surf. Sci. Adv.* **2021**, *4*, 100068.
[6] N. Oliva, J. Conde, K. Wang, N. Artzi, *Acc. Chem. Res.* **2017**, *50*, 669.
[7] J. He, M. Shi, Y. Liang, B. Guo, *Chem. Eng. J.* **2020**, *394*, 124888.
[8] P. Bilalis, D. Skoulas, A. Karatzas, J. Marakis, A. Stamogiannos, C. T. Simblouli, E. Sereti, E. Stratikos, K. Dimas, D. Vlassopoulos, H. Latrou, *Biomacromolecules* **2018**, *19*, 3840.
[9] S. Nejati, E. Mohseni Vadeghani, S. Khorshidi, A. Karkhaneh, *Eur. Polym. J.* **2020**, *122*, 109353.
[10] A. B. Jindal, *Int. J. Pharm.* **2017**, *532*, 450.
[11] H. Meng, S. Yang, Z. Li, T. Xia, J. Chen, Z. Ji, H. Zhang, X. Wang, S. Lin, C. Huang, Z. Hong Zhou, J. I. Zink, A. E. Nel, *ACS Nano* **2011**, *5*, 4434.
[12] E. Ben-Akiva, R. A Meyer, H. Yu, J. T. Smith, D. M. Pardoll, J. J. Green, *Sci. Adv.* **2020**, *6*, eaay9035.
[13] J. A. Champion, S. Mitragotri, *Proc. Natl. Acad. Sci. U. S. A.* **2006**, *103*, 4930.
[14] C. Kinnear, T. L. Moore, L. Rodriguez-Lorenzo, B. Rothen-Rutishauser, A. Petri-Fink, *Chem. Rev.* **2017**, *117*, 11476.
[15] C. Chen, R. A. L. Wylie, D. Klinger, L. A. Connal, *Chem. Mater.* **2017**, *29*, 1918.
[16] V. Kozlovskaya, B. Xue, E. Kharlampieva, *Macromolecules* **2016**, *49*, 8373.
[17] J. L. Perry, K. P. Herlihy, M. E. Napier, J. M. DeSimone, *Acc. Chem. Res.* **2011**, *44*, 990.
[18] D. K. Hwang, J. Oakey, M. Toner, J. A. Arthur, K. S. Anseth, S. Lee, A. Zeiger, K. J. Van Vliet, P. S. Doyle, *J. Am. Chem. Soc.* **2009**, *131*, 44994.
[19] Sharratt, W. N. Sharratt, A. Brooker, E. S. J. Robles, J. T. Cabral, *Soft Matter* **2018**, *14*, 4453.
[20] J. A. Champion, Y. K. Katare, S. Mitragotri, *Proc. Natl. Acad. Sci. U. S. A.* **2007**, *104*, 11901.
[21] L. Song, X. Chen, X. Huang, L. Zhong, X. Jiang, X. Zhang, *Langmuir* **2019**, *35*, 90449.
[22] I. Sadeghi, X. Lu, M. Sarmadi, R. Langer, A. Jaklenec, *Small Methods* **2022**, *6*, 2200232.

[23] Y.-C. Lo, Y.-J. Chiu, H.-F. Tseng, J.-T. Chen, *Langmuir* **2017**, *33*, 12300.
[24] J. J. Richardson, J. Cui, M. Björnmalm, J. A. Braunger, H. Ejima, F. Caruso, *Chem. Rev.* **2016**, *116*, 14828.
[25] J. Borges, J. F. Mano, *Chem. Rev.* **2014**, *114*, 8883.
[26] O. Shchepelina, V. Kozlovskaya, E. Kharlampieva, W. Mao, A. Alexeev, V. V. Tsukruk, *Macromol. Rapid Commun.* **2010**, *31*, 2041.
[27] Y. Wang, A. S. Angelatos, F. Caruso, *Chem. Mater.* **2008**, *20*, 848.
[28] D. Wu, F. Xu, B. Sun, R. Fu, H. He, K. Matyjaszewski, *Chem. Rev.* **2012**, *112*, 3959.
[29] C. Tan, M. J. Selig, M. C. Lee, A. Abbaspourrad, *Food Hydrocolloids* **2018**, *84*, 200.
[30] Q. Wei, H. Ai, Z. Gu, *Colloids Surf., B* **2011**, *85*, 63.
[31] A. Abreu, J. Carvalho, A. Tedesco, M. Beltrame Junior, A. Simioni, *J. Mater. Res.* **2019**, *34*, 1353.
[32] B. Xue, W. Wang, J.-J. Qin, B. Nijampatnam, S. Murugesan, V. Kozlovskaya, R. Zhang, S. E. Velu, E. Kharlampieva, *Acta Biomater.* **2017**, *58*, 386.
[33] M. Arjama, S. Mehnath, M. Jeyaraj, *Int. J. Biol. Macromol.* **2022**, *213*, 435.
[34] J. Chen, V. Kozlovskaya, A. Goins, J. Campos-Gomez, M. Saeed, E. Kharlampieva, *Biomacromolecules* **2013**, *14*, 3830.
[35] X. Liang, V. Kozlovskaya, Y. Chen, O. Zavgorodnya, E. Kharlampieva, *Chem. Mater.* **2012**, *24*, 3707.
[36] N. Gupta, V. Kozlovskaya, M. Dolmat, E. Kharlampieva, *Langmuir* **2019**, *35*, 10910.
[37] V. Kozlovskaya, M. Dolmat, E. Kharlampieva, *ACS Appl. Polym. Mater.* **2021**, *3*, 2274.
[38] B. Xue, V. Kozlovskaya, M. A. Sherwani, S. Ratnayaka, S. Habib, T. Anderson, M. Manuvakhova, L. Klampfer, N. Yusuf, E. Kharlampieva, *Biomacromolecules* **2018**, *19*, 4084.
[39] B. Xue, V. Kozlovskaya, F. Liu, J. Chen, J. F. Williams, J. Campos-Gomez, M. Saeed, E. Kharlampieva, *ACS Appl. Mater. Interfaces* **2015**, *7*, 13633.
[40] V. Kozlovskaya, B. Xue, M. Dolmat, E. Kharlampieva, *Macromolecules* **2021**, *54*, 9712.
[41] H. Zhu, E. W. Stein, Z. Lu, Y. M. Lvov, M. J. McShane, *Chem. Mater.* **2005**, *17*, 2323.
[42] V. Kozlovskaya, W. Higgins, J. Chen, E. Kharlampieva, *Chem. Commun.* **2011**, *47*, 8352.
[43] V. Kozlovskaya, S. Yakovlev, M. Libera, S. A. Sukhishvili, *Macromolecules* **2005**, *38*, 4828.
[44] V. Kozlovskaya, E. Kharlampieva, M. L. Mansfield, S. A. Sukhishvili, *Chem. Mater.* **2006**, *18*, 328.
[45] I. Haq, E. Matijevic, K. Akhtar, *Chem. Mater.* **1997**, *9*, 2659.
[46] M. Augustin, D. Fenske, I. Bardenhagen, A. Westphal, M. Knipper, T. Plaggenborg, J. Kolny-Olesiak, J. Parisi, *Beilstein J. Nanotechnol.* **2015**, *6*, 47.
[47] L. Dimesso, L. Heider, H. Hahn, *Solid State Ionics* **1999**, *123*, 39.
[48] S. Ren, X. He, X. Qu, I. S. Humail, Y. Li, *Mater. Sci. Eng., A* **2007**, *444*, 112.
[49] E. S. Toberer, T. D. Schladt, R. Seshadri, *J. Am. Chem. Soc.* **2006**, *128*, 1462.
[50] Z. S. Li, P. T. Liang, N. S. Cai, *Faraday Discuss.* **2016**, *192*, 197.
[51] T.-Z. Ren, Z.-Y. Yuan, W. Hu, X. Zou, *Microporous Mesoporous Mater.* **2008**, *112*, 467.
[52] W. Zhang, H. Xin, R. Li, H. He, *Asian J. Chem.* **2013**, *25*, 3769.
[53] G. Cai, P. Yan, L. Zhang, H.-C. Zhou, H. L. Jiang, *Chem. Rev.* **2021**, *121*, 12278.
[54] P. Kuhn, A. Forget, D. Su, A. Thomas, M. Antonietti, *J. Am. Chem. Soc.* **2008**, *130*, 13333.
[55] K. Turkova, D. Slizovskiy, M. Tangstad, *ISIJ Int.* **2014**, *54*, 1204.
[56] S. Fritsch, J. Sarrias, A. Rousset, G. U. Kulkarni, *Mater. Res. Bull.* **1998**, *33*, 1185.
[57] S. Lei, K. Tang, Z. Fang, Q. Liu, H. Zheng, *Mater. Lett.* **2006**, *60*, 53.
[58] A. Fauzi, B. Lidia, R. Ratnawulan, R. Ramli, *J. Phys.: Conf. Ser.* **2019**, *1185*, 012032.
[59] V. Kozlovskaya, Y. Wang, W. Higgins, J. Chen, Y. Chen, E. Kharlampieva, *Soft Matter* **2012**, *8*, 9828.
[60] V. Kozlovskaya, J. Alexander, Y. Wang, T. Kuncewicz, X. Liu, B. Godin, E. Kharlampieva, *ACS Nano* **2014**, *8*, 5725.
[61] C. Ortiz, G. Hadziioannou, *Macromolecules* **1999**, *32*, 780.
[62] P. Knappe, R. Bienert, S. Weidner, A. F. Th¨unemann, *Polymer* **2010**, *51*, 1723.
[63] Y. Wang, A. S. Angelatos, D. E. Dunstan, F. Caruso, *Macromolecules* **2007**, *40*, 7594
[64] X. Sun, G. Wang, H. Zhang, S. Hu, X. Liu, J. Tang, Y. Shen, *ACS Nano* **2018**, *12*, 6179.
[65] D. Yin, H. Wen, G. Wu, S. Li, C. Liu, H. Lu, D. Liang, *Soft Matter* **2020**, *16*, 2301.
[66] M. N. Holme, I. A. Fedotenko, D. Abegg, J. Althaus, L. Babel, F. Favarger, R. Reiter, R. Tanasescu, P.-L. Zaffalon, A. Ziegler, B. Müller, T. Saxer, A. Zumbuehl, *Nat. Nanotechnol.* **2012**, *7*, 536.
[67] N. Korin, M. Kanapathipillai, B. D. Matthews, M. Crescente, A. Brill, T. Mammoto, K. Ghosh, S. Jurek, S. A. Bencherif, D. Bhatta, A. U. Coskun, C. L. Feldman, D. D. Wagner, D. E. Ingber, *Science* **2012**, *337*, 738.
[68] J. Yu, W. Ha, J. N. Sun, Y. P. Shi, *ACS Appl. Mater. Interfaces* **2014**, *6*, 19544.
[69] X. Qi, W. Wei, J. Li, Y. Liu, X. Hu, J. Zhang, L. Bi, W. Dong, *ACS Biomater. Sci. Eng.* **2015**, *1*, 1287.
[70] V. Kozlovskaya, J. Chen, C. Tedjo, X. Liang, J. Campos-Gomez, J. Oh, M. Saeed, C. Lungu, E. Kharlampieva, *J. Mater. Chem. B* **2014**, *2*, 2494.